

## Article

# Optimizing Tensile Properties and Hardness of Inconel 718 by Cold Rolling

Wakshum Mekonnen Tucho , Anders Thon Sletsjøe <sup>†</sup>, Navid Sayyar  and Vidar Hansen

Department of Mechanical and Structural Engineering and Materials Science, Faculty of Science and Technology, University of Stavanger, 4036 Stavanger, Norway; sletsjoe.anders@gmail.com (A.T.S.); navid.sayyar@uis.no (N.S.); vidar.hansen@uis.no (V.H.)

\* Correspondence: wakshum.m.tucho@uis.no

<sup>†</sup> Current address: Vipe 21 AS, Luramyrvæien 23, 4313 Sandnes, Norway.

**Abstract:** The as-received commercial Inconel 718 material was solid solution heat treated (ST), cold-rolled (CR), and precipitation-hardened (PH) to investigate the effects of deformation on the tensile properties, hardness, and texture. Three sets of specimens (0%, 20%, and 50% CR) were ST at 1100 °C/1 h, CR, and aged (720 °C/8 h + 650 °C/8 h) for the analysis. The ultimate tensile strength (UTS), 0.2% yield strength (YS), and elongation of 50% deformed condition were 1645 MPa, 1512 MPa, and 3.8%, respectively. The 20% deformation resulted in a balanced UTS (1348 MPa), YS (1202 MPa), and elongation (11%). The contribution of precipitation hardening to the strength decreased, while the contribution of CR increased with an increasing percentage of deformation. As the level of deformation increased, the size and quantity of  $\gamma''$  decreased proportionally. The CR specimens produced a high density of nano/micro twins with twin planes oriented perpendicular to the RD-ND surface. The gradient of crystal orientation and internal features of large austenitic grains were generated by their preferred rotation. The cross-slip of screw dislocations induced a complete  $\beta$ -fiber consisting of  $\{110\}\langle 112\rangle$ ,  $\{112\}\langle 111\rangle$ , and  $\{123\}\langle 634\rangle$ , with doubled intensity at the higher deformation. Additionally, the specimens were highly susceptible to the twinning-induced orientation emerged by a predominant  $\langle 110\rangle//ND$ . In the as-deformed condition, an incomplete but intense  $\alpha$ -fiber, clustered between  $\{110\}\langle 001\rangle$  and  $\{110\}\langle 112\rangle$ , was characterized. Apart from achieving the highest strength, the current work demonstrates the effects of CR on the material strength without the complex influences of  $\delta$  precipitates.

**Keywords:** tensile properties; microstructure; hardness; texture; microscopy; characterization



**Citation:** Tucho, W.M.; Sletsjøe, A.T.; Sayyar, N.; Hansen, V. Optimizing Tensile Properties and Hardness of Inconel 718 by Cold Rolling. *Metals* **2024**, *14*, 455. <https://doi.org/10.3390/met14040455>

Academic Editors: Andrea Di Schino, Claudio Testani and Xiao-Wu Li

Received: 1 March 2024

Revised: 1 April 2024

Accepted: 10 April 2024

Published: 12 April 2024



**Copyright:** © 2024 by the authors. Licensee MDPI, Basel, Switzerland. This article is an open access article distributed under the terms and conditions of the Creative Commons Attribution (CC BY) license (<https://creativecommons.org/licenses/by/4.0/>).

## 1. Introduction

Inconel 718 is a precipitation-strengthened nickel-based superalloy with high strength, excellent creep, and corrosion resistance [1,2]. The alloy is an ideal choice in a wide range of service temperatures, especially in energy and aviation sectors, due to its stable mechanical properties at temperatures as high as 650 °C [3,4]. The as-produced Inconel 718 superalloy generally consists of an austenite, face-centered cubic (FCC) matrix and some primary segregated phases, mainly laves and carbides. Before application, the segregated phases, especially laves, need to be dissolved as they have detrimental effects on the mechanical properties. An optimum microstructure and mechanical strength of the alloy can be obtained by performing two steps of post-fabrication heat treatments, which are solid solution heat treatment (ST) and aging (also known as precipitation hardening) [5–8]. After the successive heat treatments, the main desired phases to precipitate in the austenite matrix of the alloy are the FCC L1<sub>2</sub>-ordered Ni<sub>3</sub>(Al,Ti)  $\gamma'$  and the bct D022-ordered Ni<sub>3</sub>Nb  $\gamma''$ . The latter ( $\gamma''$ ) is regarded as the main strengthening phase with a ratio of 4:1 compared to the former ( $\gamma'$ ). The other phase precipitated under a certain temperature range in Inconel 718 is the  $\delta$  phase, which is stable unlike the metastable  $\gamma''$  phase. The  $\delta$  phase has an

orthorhombic (D0a) crystal structure with a similar stoichiometry of Ni<sub>3</sub>Nb as that of  $\gamma''$ , and it is often regarded as another strengthening phase in Inconel 718 [4,9].

As a preferred material in the oil and gas industries for deep downhole drilling components, Inconel 718 is required to have a high tensile strength of over 1400 MPa and moderate ductility to withstand high-pressure and corrosive environments at relatively lower temperatures [10]. To meet these requirements, Inconel 718 can be strengthened by combining a heat treatment with work hardening via cold rolling. Cold rolling introduces dislocation networks and vacancies, which can enhance material properties, such as the tensile strength, creep resistance, and hardness, but reduce ductility [11–13]. Material properties are, however, affected by the distribution and morphology of the hardening phases, including  $\gamma'$ ,  $\gamma''$ , and  $\delta$ . It is thus important to understand how cold rolling affects the precipitation of these phases. Cold rolling results in plastic deformation, leading to changes in the morphology of grains and the grain boundary regions [14–16]. In addition to altering lattice defects, deformation is responsible for the elongation of grains and the internal structure of the grains. During cold rolling, most of the grains tend to be reoriented with respect to the directions of the stresses that are applied. These changes are normally expected to affect the nucleation, distribution, and morphology of the precipitation hardening in Inconel 718 [1].

Most of the early and recent reports [12,16–22] related to the cold rolling of Inconel 718 studied the nucleation, growth, morphology, and quantification of  $\delta$  precipitates and the effects on the mechanical properties [12,19,20] after solid solution heat treatment below the  $\delta$ -phase solvus temperature (between 1005 and 1015 °C [23]). According to these reports, the nucleation sites and precipitation of the  $\delta$  phase can be enhanced, followed by the depletion of Nb that greatly reduces the number and size of  $\gamma''$  precipitates because of global recrystallization and the transformation of  $\gamma''$  to the  $\delta$  phase. The increase in nucleation sites for the  $\delta$  phase is believed to be due to the growth in the fraction of grain boundaries [22]. Moreover, the cold rolling process significantly reduces the content of  $\gamma''$  with an increasing percentage of thickness reduction in the temperature ranges of solution and aging treatments that promote the precipitation of the  $\delta$  phase. The effects of the  $\delta$  phase on the material properties are, however, controversial since some reports show affirmative results [22], while other effects are considered detrimental [21]. On the positive side, the controlled precipitation (quantity and morphology) of the  $\delta$  phase is found to promote recrystallization, block dislocation motion, and retard grain growth, which leads to improved ductility [2,15,16,19,21,24,25]. On the contrary, the  $\delta$  phase (depending on the size and quantity) is brittle and can adversely affect the plasticity and impact the toughness of Inconel 718 [21,25–27]. Large quantities and a continuously decorated acicular  $\delta$  phase along the grain boundaries of Inconel 718 are unacceptable, for example, for oil and gas industry applications as they are prone to initiating and propagating cracking [28], especially in marine environments. According to the studies by deBarbadillo and colleagues [22,28], the amount of  $\delta$  phases along the grain boundaries directly correlates with hydrogen cracking susceptibility because it promotes interface decohesion between the  $\delta$  phase and matrix. This reminds us to avoid precipitation of the  $\delta$  phase or keep it to a minimum level in the alloy during the post-fabrication processing. Additionally, the presence of the  $\delta$  phase complicates our understanding of the effects of the main hardening phases ( $\gamma''$  and  $\gamma'$ ) under the deformation process. Given these factors, it is worth investigating the effects of cold rolling on the microstructure and mechanical properties in the absence of the  $\delta$  phase.

Identifying the strong textures formed during thermomechanical deformations and strain recrystallization and their influence on the overall performance of the materials has been a topic of interest in recent decades. The textures have the potential to impact precipitation behavior, structure rebuilding during heat treatment, and strengthening. Microstructural heterogeneity can be created through the activation of twin variants at different degrees of deformation [29]. The combination of dislocation and nano-twinning, increased dominance of orientations such as Brass in FCC alloys, and stacking faults at a high degree of deformation result in a monotonic increase in tensile strength and a

decrease in ductility in polycrystalline alloys [14,30,31]. The physical mechanisms involved in the formation of the microstructure can be studied to a significant extent using the Electron Back-Scattered Diffraction (EBSD) technique and the principles of quantitative texture analysis and Transmission Electron Microscopy (TEM). Characterizing the changes in deformation mechanisms, including dislocation slip and twinning, is important as they affect the evolution of the microstructure and mechanical features [32].

This study examines the impact of cold rolling on Inconel 718, specifically how it affects the material's microstructural properties, crystallographic orientation, and mechanical features. The solid solution heat treatment temperature was chosen to prevent the formation of the  $\delta$  phase, allowing for a clear understanding of the effects of the primary hardening precipitates during cold rolling. The research work conducted for this study was partly based on the second co-author's master's thesis project [33].

## 2. Experimental Methods

### 2.1. The Materials

The initial material was Inconel 718 comprising 7/8" bolts and nuts supplied by Scandinavian Fittings and Flanges, located in Sandnes, Norway. The composition of Inconel 718 alloy includes, 17.86 Cr, 5.02 Nb, 2.99 Mo, 0.96 Ti, 0.51 Al, 0.05 Cu, 0.07 Mn, 0.014 C, 0.06 Si, 0.008 P, 0.0025 B, 0.0005 S and with Ni comprises the balance in wt.%. According to the datasheet obtained from the supplier, the material was produced by the VIM + VAR (vacuum induction melting + vacuum arc remelting) method. After production, the specimens were solution-annealed at 1030 °C for 1.5 h (water quenched) and then precipitation-hardened at 780 °C for 6.3 h (air-cooled). Finally, the threads of the bolts and nuts were formed by cold rolling. Here, the corresponding specimens will be called original condition (OC). The microstructure of the initial material is shown in Figure 1. The OC specimen consists of equiaxed grains, numerous annealing twins, and some segregated phases along the grain boundaries and within the grains (Figure 1a). An Energy-Dispersive Spectroscopy (EDS) analysis showed that the particles are rich in Nb and Ti, indicating a carbide-type phase. Furthermore, the TEM image (Figure 1b) reveals hardening precipitates, mainly the  $\gamma''$  phase, with an average length of 51 nm.

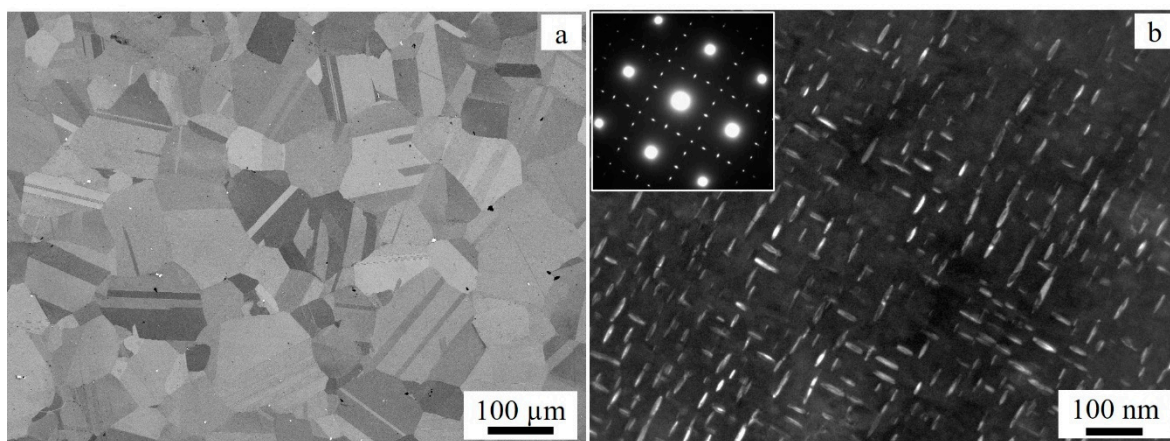


**Figure 1.** The microstructure of the initial material's (a) Scanning Electron Microscopy (SEM) image and (b) TEM dark field image, showing  $\gamma''$  phase precipitates. The insert in (b) is a diffraction pattern in the [100] zone axis.

### 2.2. Heat Treatment and Cold Rolling

The specimens for the tests were obtained by machining the bolts (OC) to a rectangular shape with a length of 134–145 mm, a width of 9.5–14.3 mm, and a thickness of 4.7–5.7 mm. For the experimental investigations, the machined OC specimens were subjected to heat treatment to attain a homogeneous state. This was achieved by performing a solid solution heat treatment (ST) at 1100 °C for 1 h followed by water quenching. The heat treatments

were performed in a Nabertherm furnace equipped with a K-type thermocouple. The heat treatment scheme chosen was based on the best ST heat treatment results obtained in a previous study of Inconel 718 [34]. The study revealed that at 1100 °C/3 h ST, most of the laves phase particles (enriched in Nb) were dissolved, and Nb atoms were evenly distributed in the matrix, allowing for the sufficient nucleation and precipitation of hardening phases. Moreover, 1100 °C is well above the solvus temperature of the  $\delta$  phase. For the ST operations, the specimens were introduced after stabilizing the furnace to the target temperatures to avoid undesirable phase transformations at lower temperatures. The hardening phases and other segregated phases were believed to be entirely or partially dissolved, and the material was nearly attained in a strain-free condition. In addition, there might be some grain coarsening and the material might become softer than the starting material (OC). The specimen at this stage is referred to as a homogenized condition or D0. The ST (D0) specimens were then cold-rolled and precipitation-hardened to analyze the effects of deformation on the mechanical properties.

The homogenized specimens (D0) were then divided into three sets based on the level of deformation to be performed. These were undeformed (0%) and 20% and 50% cold-rolled. Each set was further divided into two groups—one group was subjected to two stages of aging, and the other group was tested without aging. The aged specimens were suffixed with the letter 'A' to indicate aging. Cold rolling was carried out using a Schmitz cold rolling mill. After several passes, the thickness was reduced to 4.15–4.62 mm and 2.59–2.81 mm for the 20% and 50% reduction, respectively.

Figure 2 shows the schematic of the specimens' coordinates, i.e., normal (loading), transverse, and rolling directions denoted as ND, RD, and TD, respectively. The rolling direction was parallel to the longer axis of the specimens. To provide a clear view of the microstructure in three dimensions, EBSD maps on each sample were created from the rolling plane (RD-TD) and from the plane normal to the transverse direction (ND-RD). Large and small area acquisitions were carried out to study the grains' preferred orientations and grain boundaries. The diffraction data were subjected to grain dilation clean-up by the TSL-OIM program to diminish the noise effect in the orientation maps. The IPF maps of the deformed specimens were noise-removed through one to three iterations of grain dilation with a minimum grain size of 2 pixels and a grain tolerance angle of 5 degrees. The EBSD data were further processed with the ATEX software (version 4.12) (Analysis Tools for Electron and X-ray Diffraction; Beausir and Funderberger, 2017 [35]) to determine the texture evolution with respect to the deformation levels through the pole figures and orientation distribution functions (ODFs). The harmonic series method was used for texture calculations. Presuming that the rolled FCC material had orthonormal symmetry, the domain of the Euler space was decreased to  $0^\circ < \varphi_1, \Phi, \varphi_2 < 90^\circ$ .

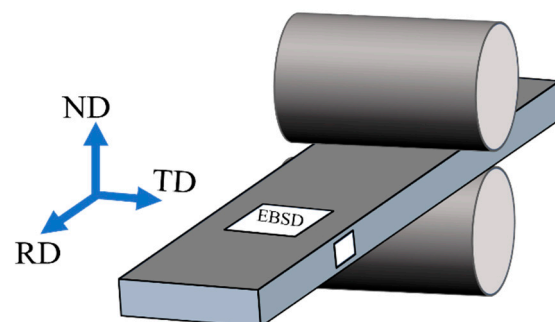


**Figure 2.** Schematic representation of rolling plate and corresponding workshop axes.

The Inconel 718 specimens underwent a precipitation hardening treatment using two successive heat treatments, which are typical for conventionally fabricated Inconel 718 specimens. The furnace was pre-heated to the aging temperature, and then the specimens were introduced. The aging treatment was conducted at 720 °C for 8 h, followed by a cooling period where the furnace temperature was reduced to 650 °C for another 8

h, in accordance with AMS 5662 [36], which is the standard for conventional Inconel 718 material. At the end of the soaking period, the specimens were removed from the furnace and cooled in the air. Information about the specimens is available in Table 1. Moreover, the heat treatment regimens and rolling are illustrated in Figure 3.

**Table 1.** Descriptions of specimens.

Sample ID	ST	Def. (%)	PH	
	1100 °C /1 h		720 °C /8 h	650 °C /8 h
D0	Yes	0	No	No
D0A	Yes	0	Yes	Yes
D20	Yes	20	No	No
D20A	Yes	20	Yes	Yes
D50	Yes	50	No	No
D50A	Yes	50	Yes	Yes
OC				

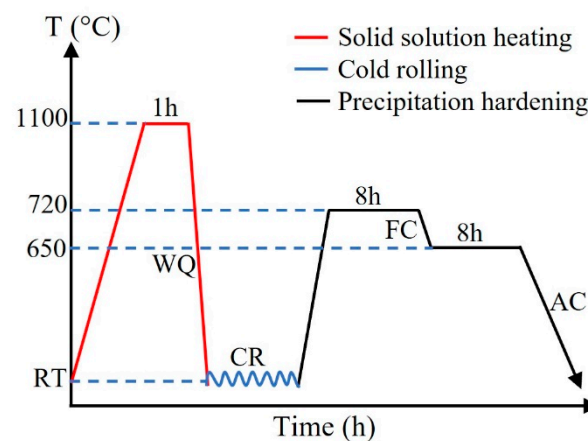


**Figure 3.** Schematic profile of heat treatment regime and cold rolling, where  $T \equiv$  temperature, WQ  $\equiv$  water quenching, AC  $\equiv$  air cooling, FC  $\equiv$  furnace cooling, and CR  $\equiv$  cold rolling.

### 2.3. Characterization of Microstructure, Texture, and Phases

The microstructure, composition, and fracture surfaces of the specimens were analyzed with SEM using a Gemini SUPRA 35VP (Carl Zeiss, Jena, Germany) equipped with EDAX EDS. The crystallographic orientation was studied using EBSD equipped on an SEM using a TSL-OIM orientation imaging microscope system for analysis. Specimen preparation for the microstructure analysis consisted of mechanical grinding, fine polishing, and ultra-polishing with OP-S colloidal silica. EBSD mapping was performed at 20 kV, a working distance of 25 mm, a tilt angle of 70°, a scan step of 0.5–2  $\mu\text{m}$ , and a magnification of 100/200 $\times$ .

The investigation of phases and lattice defects was carried out using a JEOL-2100 TEM with a LaB<sub>6</sub> filament (Tokyo, Japan). The microscope operates at 200 kV and is equipped with a CMOS XAROSA camera from EMSIS GmbH (Münster, Germany), which is controlled by RADIUS software (Version 2.2). The tool modules incorporated in RADIUS allow for measurements to be conducted down to an atomic level. For the observation with TEM, thin foils were mechanically thinned down to a thickness of about 100  $\mu\text{m}$  from the ND-TD surface. Then, 3 mm disks were punched from the thin foils. Finally, the disks were electropolished using a dual jet polishing system, Struers TENUPO-5, from Struers in Ballerup, Denmark. The electropolishing was performed at 15 V and  $-30$  °C in an electrolyte solution of 80% methanol and 20% perchloric acid.

#### 2.4. Hardness Test

Vickers hardness tests were performed on the RD-ND plane, which runs parallel to the rolling direction. The tests were conducted under a 5 kg load and a 10 s dwell time with the help of an Innovatest automatic hardness tester (Maastricht, the Netherlands). This allowed for multiple indentations to be performed in a controlled and precise manner. The interval between adjacent indentations was set to at least 3 times the average length of the diagonal according to the standard specifications stated in ISO 6507-01 [37]. To prevent edge effects, the indentations were made at over 2.5 times the average length of the diagonal from the edges. To ensure accuracy, more than 70 imprints were made on each test specimen.

#### 2.5. Tensile Test

The specimens used in the tensile tests were obtained by machining the bolts (OC) into a rectangular shape with a length of 134–145 mm, a width of 9.5–14.3 mm, and a thickness of 4.7–5.7 mm. The uniaxial tensile tests were conducted at room temperature and parallel to the rolling direction using an Instron 5985 universal testing machine (Norwood, MA, USA) in accordance with test method A1 in ISO standard NS-EN ISO 6892-1:2019 [38]. The tests were conducted at a strain rate of  $0.00025 \text{ s}^{-1}$ . The measurement of elongation was carried out with the help of an external clip-on extensometer. The CNC machine used for machining the specimens was the Mazak Vertical Center, Smart 430 A (Florence, SC, USA). The geometry of the specimens tested is depicted in Figure 4. For the 20% and 50% deformed cases, three tensile specimens were prepared. However, due to a shortage of material, only one specimen was available for the undeformed (D0A) case.

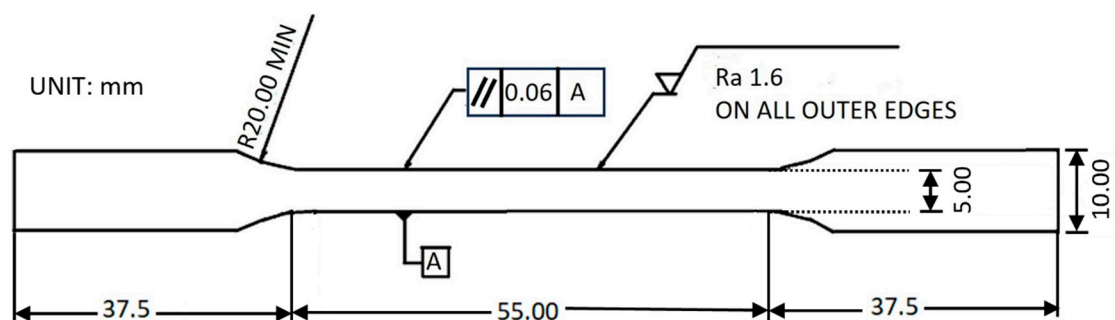


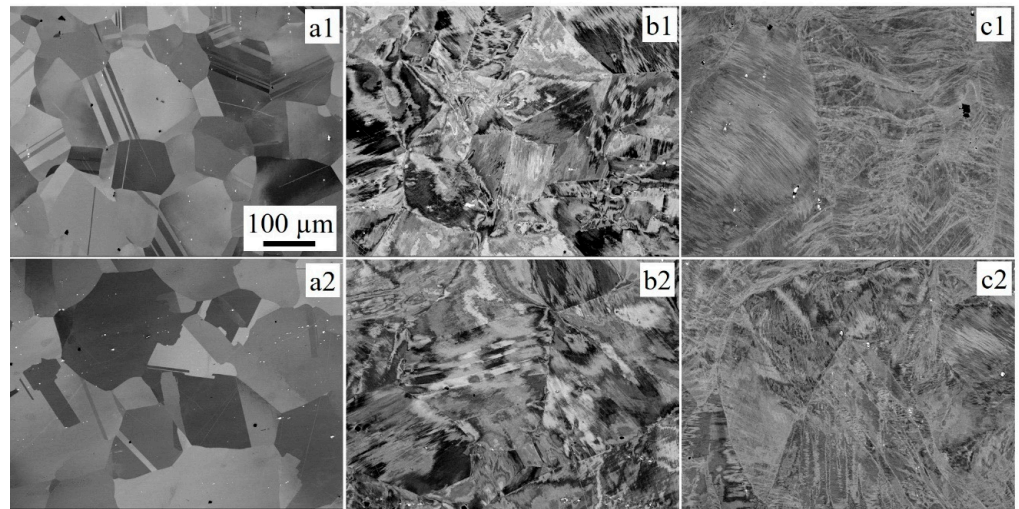
Figure 4. Schematic of tensile specimens.

### 3. Results

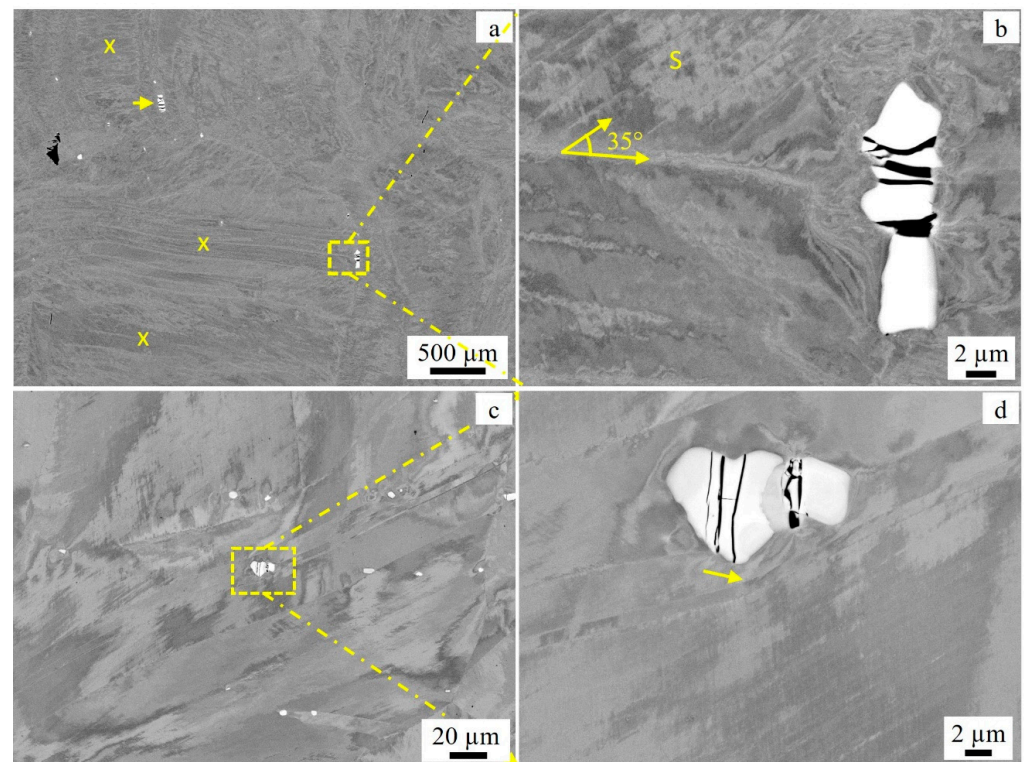
#### 3.1. Microstructure

The microstructures of the specimens prepared from the RD-TD planes and subjected to different conditions are depicted in Figure 5. The upper row displays images taken before aging, while the lower row displays images taken after aging. The images from left to right correspond to 0%, 20%, and 50% deformed specimens, respectively, in both rows. There are no noticeable differences in the grain structure between the specimens before and after aging for the same deformation. Generally, the aging temperatures of  $720 \text{ }^\circ\text{C}$  and  $620 \text{ }^\circ\text{C}$  are not sufficiently high to cause recrystallization that leads to changes in grain structures, as demonstrated in previous reports [34]. At 0% deformation, both specimens D0 (Figure 5(a1)) and D0A (Figure 5(a2)) show similar features with twins and grains. At 20% (b1 and b2) and 50% (c1 and c2) deformation, the microstructures appear similar at the given magnification and resolution. The cold work process stressed the microstructures to a level that makes it difficult to distinguish the grain boundaries from the contrast. The equiaxed grains were replaced by deformed grains before the rolling process. Most annealing twins formed by the ST were eliminated during the cold rolling process. However, both sets of specimens (20% and 50% deformed) show features that appear as strips across grains. Figure 6 shows typical examples of such strips. The TEM

observations revealed that these strips are deformation twins that formed due to the cold rolling process, as presented in Section 4.



**Figure 5.** SEM-backscattered images showing the microstructure of the specimens before aging (top row) and after aging (bottom row) for 0% deformed (a1,a2), 20% deformed (b1,b2), and 50% deformed (c1,c2) specimens. All of the images were taken at the same magnification (100×), and the scale bar shown in (a1) applies to the rest of the images as well.



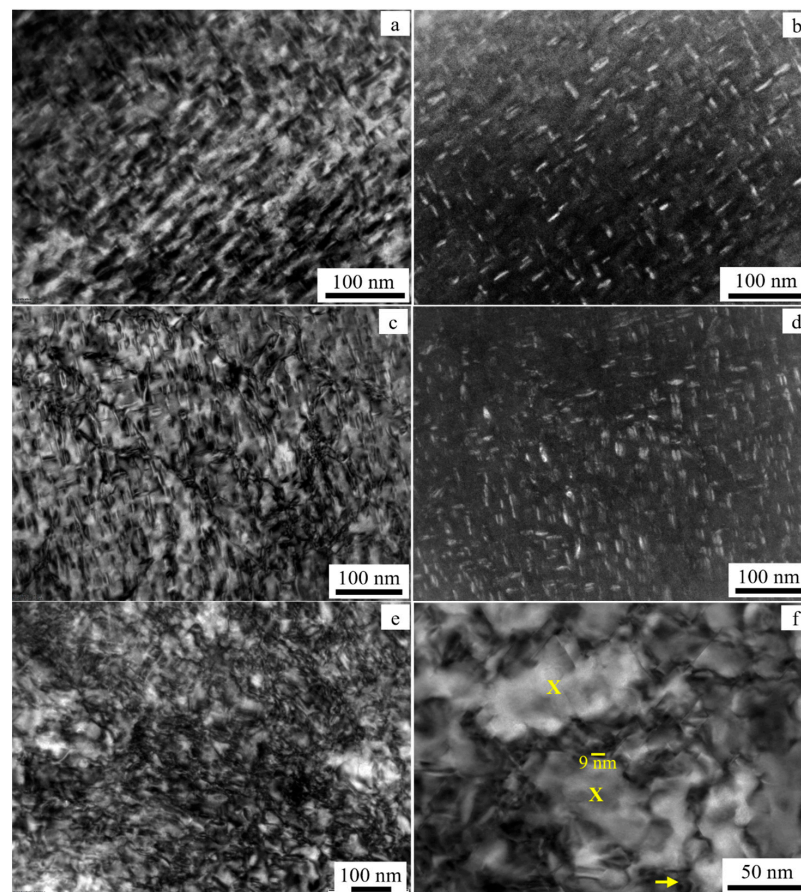
**Figure 6.** SEM-backscattered images of 50% deformed and aged (D50A) specimens (a) at a low magnification and (b) at a high magnification. (c,d) show similar images of D20A. The 'X' marks in (a) indicate regions with elongated stripes appearing parallel to the direction of rolling, while 'S' shows some of the shear bands that are oriented at about 35° relative to the rolling direction. The approximate locations of the images in (b,d) are shown by dashed boxes in (a,c).

Figure 6 displays the microstructures of plastically deformed D50A and D20A materials. The microstructures marked by the letter X in Figure 6a consist of strips that are parallel to

the rolling direction. These strips appear to be elongated grains or twins, but their formation is hindered or blocked by a carbide particle, as indicated by the white contrast. The EDS analysis shows that the carbide particle contains 89 wt.% Nb and 7 wt.% Ti. Due to the forces applied during rolling, the carbide particles are cracked, and the cracks are oriented perpendicular to the rolling direction. The area around the carbide phase is heavily deformed, as shown in Figure 6b. Other particles also exhibit cracks at an angle relative to the rolling direction, as shown in Figure 6c,d. Figure 6d demonstrates how the rolling process dislocated the carbide particle and the strips bent around the bulged part of the particle. The cracks could be reoriented to the shown position after several passes of rolling. Additionally, there are numerous shear bands with a relative orientation of about  $35^\circ$  to the rolling direction (Figure 6b).

### 3.2. Hardening Precipitates

The phases precipitated in the aged Inconel 718 specimens were studied using TEM. Bright Field (BF) and Dark Field (DF) images were recorded and analyzed. The micrographs in Figure 7 show the precipitates in specimens that were deformed by 0% (Figure 7a,b), 20% (Figure 7c,d), and 50% (Figure 7e,f). The main hardening precipitate in Inconel 718 after the aging treatment is the  $\gamma''$  phase, which is generally nano-sized and ellipsoid in shape. However, in this study, the  $\gamma''$  precipitates were shorter and rod-shaped in the cold-rolled specimens. Another hardening phase precipitated after aging is  $\gamma'$ , which is round and finer than the  $\gamma''$  precipitates.



**Figure 7.** TEM images of  $\gamma''$  recorded with the matrix oriented in the [100] zone axis of D0A (a) BF and (b) DF; D20A (c) BF and (d) DF; and D50A (e,f) BF. The 'X' marks in the magnified image of (f) indicate local strain-free areas. An example of a precipitate is shown by an arrow in (f).

As shown in Figure 7a,b, the precipitates are uniformly distributed in the undeformed specimen. Likewise, the  $\gamma''$  precipitates in the 20% rolled specimen (Figure 7c,d) appear

dense and evenly distributed. However, the precipitates in the 50% rolled specimen (D50A) appear scattered, as shown in Figure 7e,f. The microstructure of D50A contains both high strain and strain-free regions. Examples of strained and precipitate-free regions are marked by X in Figure 7f. The strained region consists of tiny precipitates of  $\gamma''$  and dislocations that establish high-stress field regions. From these results, we can infer that the hardening precipitates in D50A are more likely to nucleate at highly strained locations than the less strained ones.

The size and quantity of precipitates can impact material strength, as previously documented [8]. In this study, several dark field TEM micrographs were obtained in a  $\langle 100 \rangle$  zone axis, and the sizes of the precipitates were measured using the tools present in the RADIUS software (Version 2.2). The size estimation was based on the measurements of 200–500 precipitates for each case. Accordingly, the size of  $\gamma''$  precipitates in OC, D0A, D20A, and D50A are  $50.7 \pm 9.3$ ,  $9.5 \pm 2.1$ ,  $12.6 \pm 3.2$ , and  $8.2 \pm 1.6$  nm., respectively. The measurement showed that the precipitates formed in the reprocessed specimens (heat-treated, rolled, and aged) are smaller than the original material by about 5-fold. A comparison of the deformed specimens with the non-deformed specimen (D0A) shows slight differences. Specifically, the average size of the  $\gamma''$  phase in D20A is larger than those in D0A by about 3 nm (35%). The  $\gamma''$  phase precipitated under the D50A condition, however, decreased by 1.3 nm (14%) and by 4.4 nm (54%) compared to D0A and D20A, respectively. This shows that the dimension of the  $\gamma''$  precipitate decreased with an increasing percentage of deformation. This agrees well with similar observations in the literature [24]. The images shown in Figure 8 are typical diffraction patterns with the matrix oriented in the  $[100]$  zone axis for (a) D0A, (b) D20A, and (c) D50A, corresponding to 0%, 20%, and 50% deformed and aged specimens, respectively, as presented in Figure 7. As documented in the literature [5,39], for the unambiguous identification of the  $\gamma''$  and  $\gamma'$  phases, the matrix ( $\gamma$  phase) must be oriented in the  $\langle 100 \rangle$  zone axis. The SADP shown in the insets of Figure 8a–c consists of strong reflections from the matrix (FCC- $\gamma$  phase) oriented in the  $[100]$  zone axis and the superimposed weaker superlattice reflections of the  $\gamma''$  (BCT) and  $\gamma'$  (primitive cubic) phases.

Since the zone axes of  $\gamma''$  are parallel with the matrix, rows of parallel spots of  $\gamma''$  are superimposed with that of the matrix, and there exists an orientation relationship between the two phases:  $(100)_{\gamma''} // (100)_{\gamma}$ ;  $[010]_{\gamma''} // [010]_{\gamma}$ . The simulated SADP of the three variants of the  $\gamma''$  phase in the  $[100]$  zone axis of the matrix is shown in Figure 8d. The white spots correspond to the matrix, whereas green, yellow, and red represent diffraction spots of the  $\gamma''$  phase variants in the  $[001]$ ,  $[010]$ , and  $[100]$  zone axes, respectively. Some of these diffraction spots are labeled with Miller indices to illustrate the overlapping of the spots (Figure 8d). The streaking of the lattice reflections of  $\gamma''$  precipitates in the  $[010]$  and  $[100]$  zone axes indicate that the precipitates are thin and ellipsoidal in shape. The spots in the  $[001]$  direction appear as a disc due to the parallel zone axis with the BCT c-axis.

Qualitatively, the strength/size of the streaking of the  $\gamma''$  precipitates of the three specimens is different, as shown in Figure 8a–c. The spots of the reciprocal lattice reflections are larger in the order of D20A, D0A, and D50A. Specifically, the reflections of the  $\gamma''$  phase corresponding to D50A are thin and short. These findings agree well with the quantitative analysis of the precipitates stated above. In the current study, the identification of  $\gamma'$  was difficult, possibly due to its small size and lower quantity in the deformed specimens.

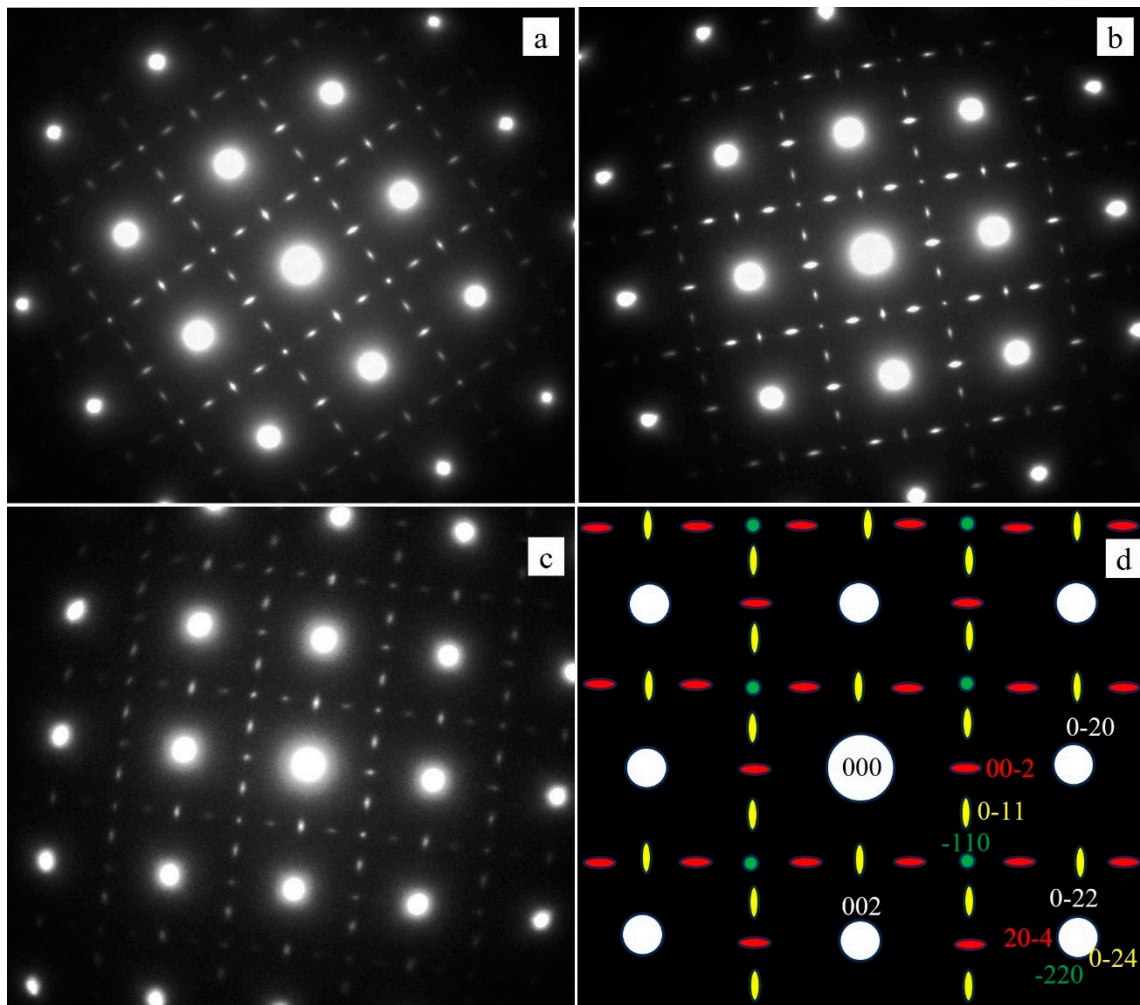


**Figure 8.** Selected Area Diffraction Pattern (SADP) of the matrix in [100] for D0A (a), D20A (b), and D50A (c) corresponding to the images shown in Figure 7a–f, respectively. (d) is the simulated SADP for the matrix [100] showing the three variants of the  $\gamma''$  phase in [001] (green), [010] (yellow), and [100] (red). The white spots in (d) are reflections from the matrix.

### 3.3. Hardness

Figure 9 displays the hardness measurements of all of the samples tested. The red and green bars represent the hardness before and after the precipitation hardening heat treatments, respectively, making it easier to visualize the effects of aging. As shown in the figure, the hardness of the specimen with zero deformation, i.e., D0, increased from  $165 \pm 4.6$  to  $430 \pm 11.3$  HV after the aging treatment (D0A). This represents a significant increase of about 265 HV or 160% in hardness due to the formation of hardening precipitates, primarily the  $\gamma''$  phase. The change in hardness can be assessed by comparing the hardness of the undeformed (D0) specimen with the hardness after the two levels of deformation (D20 and D50). A 20% deformation (D20) increased the hardness by 126 HV (76%), while a 50% deformation resulted in a 252 HV (153%) increase compared to the specimen without deformation (D0). After undergoing the aging treatment, the deformed specimens were further strengthened. The hardening precipitates strengthened D20A by 181 HV (62%) and strengthened D50A by 111 HV (27%) relative to the values before aging. In simpler terms, the 20% and 50% rolled/deformed and aged specimens demonstrated hardness increases of approximately 42 HV (10%) and 98 HV (23%), respectively, compared to D0A (0% deformed and aged).

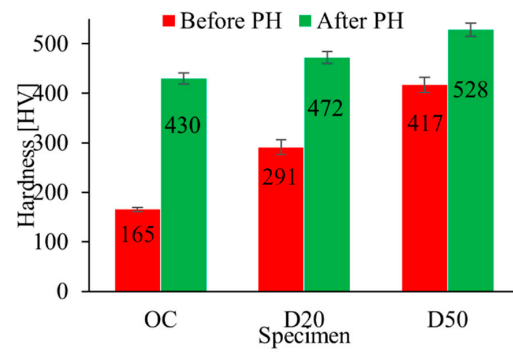


**Figure 9.** Hardness measurement. D0 represents 0% deformation, while D20 and D50 refer to specimens deformed by 20% and 50% by cold rolling, respectively. Red bars indicate hardness values before aging, while green bars show hardness values after aging. PH stands for precipitation hardening. OC (original condition) is starting material for current investigations.

### 3.4. Tensile Properties

The stress–elongation curves in Figure 10 illustrate the tensile behavior of three sets of specimens (D0A, D20A, and D50A) tested at room temperature. The inset bar chart provides a comparison of the average values for yield strength and ultimate tensile strength. The yield strength is represented by patterned bars and the ultimate tensile strength is shown with solid bars. The colors black, red, and green are used to mark the results related to D0A, D20A, and D50A, respectively. The variations in tensile properties have shown similar trends as those of hardness. The 0.2% yield strength of D20A increased by about 242 MPa (25%), while the 0.2% yield strength of D50A increased by 552 MPa (58%) relative to D0A. Similarly, the UTS of D20A and D50A exceeded the UTS of D0A by 216 MPa (19%) and 513 MPa (45%), respectively. Deformation of 50% resulted in an increment of 310 MPa (28%) in the yield strength and 297 MPa (22%) in the UTS compared to the specimens that were deformed by 20% and aged (D20A). In line with the hardness measurement, the tensile strength also increased proportionally with an increasing percentage of deformation.

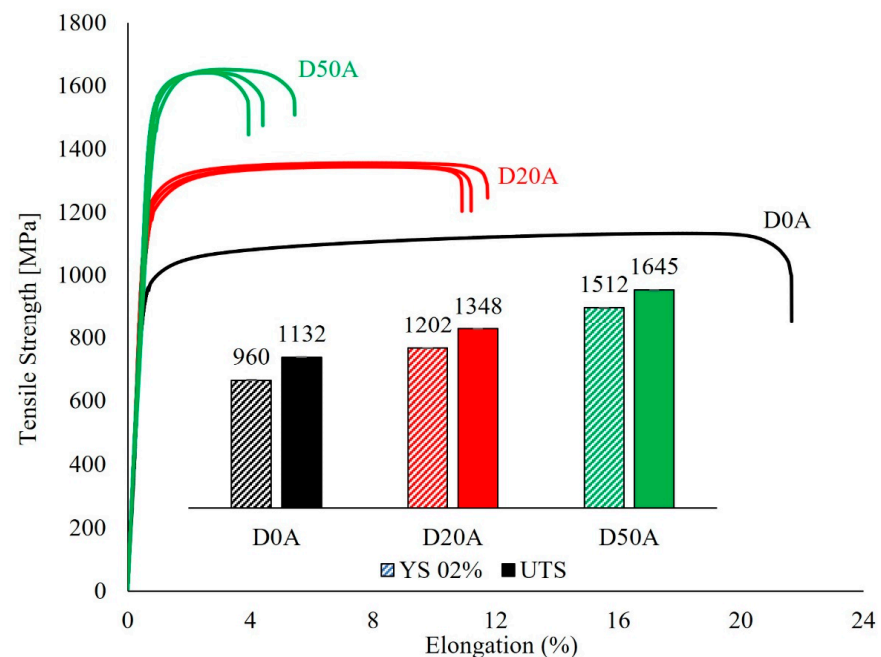


**Figure 10.** The tensile properties of the aged specimens are shown in line and bar charts. The labels at the top of the patterned bars and solid bars represent the average values of yield strength and ultimate tensile strength, respectively.

The tensile strength of Inconel 718 can be improved by rolling and aging, but this comes at a cost of reduced ductility. As we can see in Figure 10, the elongation of the material decreases as the deformation level increases. For instance, the elongation of D50A is only 3.8% compared to the elongation of D0A, which is 21.1%. This means that the reduction in elongation is roughly 17.3%. On the other hand, the D20A specimen, which was deformed by 20%, has only half the reduction in elongation compared to the undeformed D0A specimen. While deforming Inconel 718 by 50% can significantly enhance its strength, it also greatly reduces its ductility. Therefore, the choice between strength and ductility may depend on the specific service conditions. However, D20A seems to offer a balanced strength and ductility.

### 3.5. Deformation Texture Analysis

Figures 11a,d, 12a,d and 13a,d depict the RD-TD orientation maps of all specimens. To aid in visualizing the orientation, each micrograph includes a small RD-projected IPF in the top right corner. In Figure 11a, a coarse equiaxed  $\gamma$  structure and a significant number of annealing twins randomly distributed can be observed in D0 (undeformed, solution heat treated). Meanwhile, Figure 11d shows the grain structure of the undeformed but aged specimen (D0A). It is worth noting that the maximum intensity of the poles in Figure 11b,e cannot be expanded to whole materials as the number of grains sampled is an important quantity for reliable texture measurements. Additionally, the large grain size may pose a problem in obtaining reproducible results during the statistical measurements used by the EBSD technique.

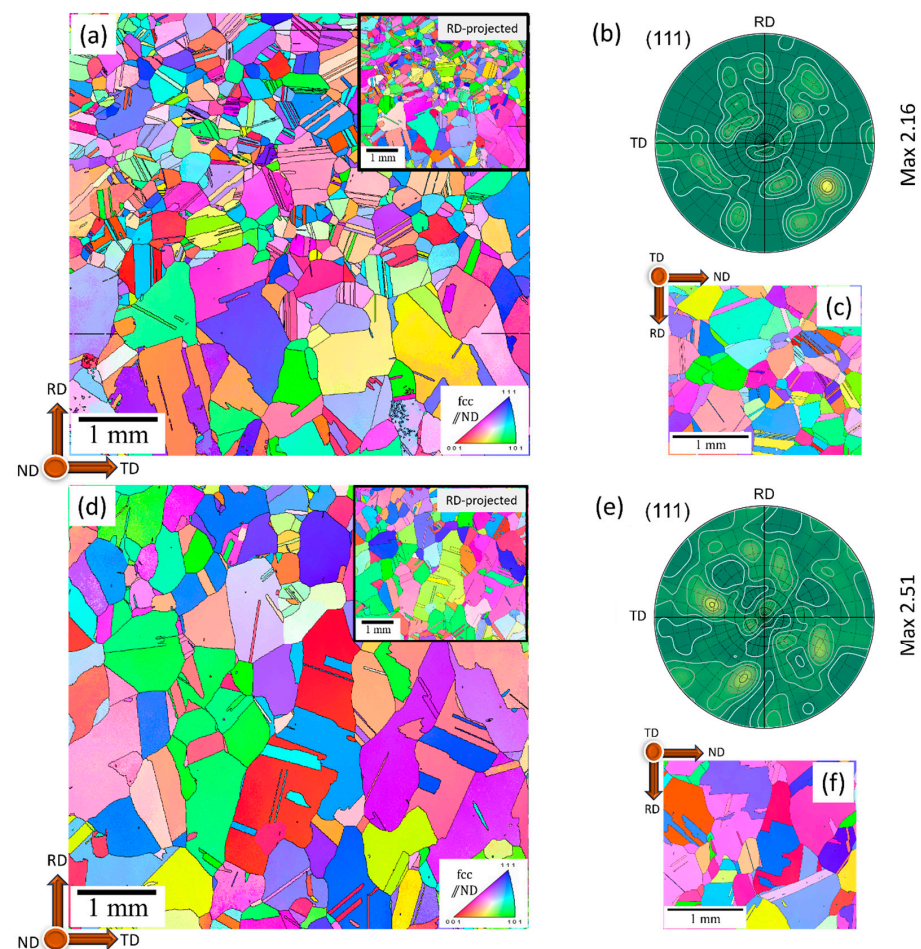


**Figure 11.** (a,d) RD-TD IPFs, (b,e) 111 pole figures, and (c,f) ND-RD IPFs corresponding to D0 and D0A, respectively.

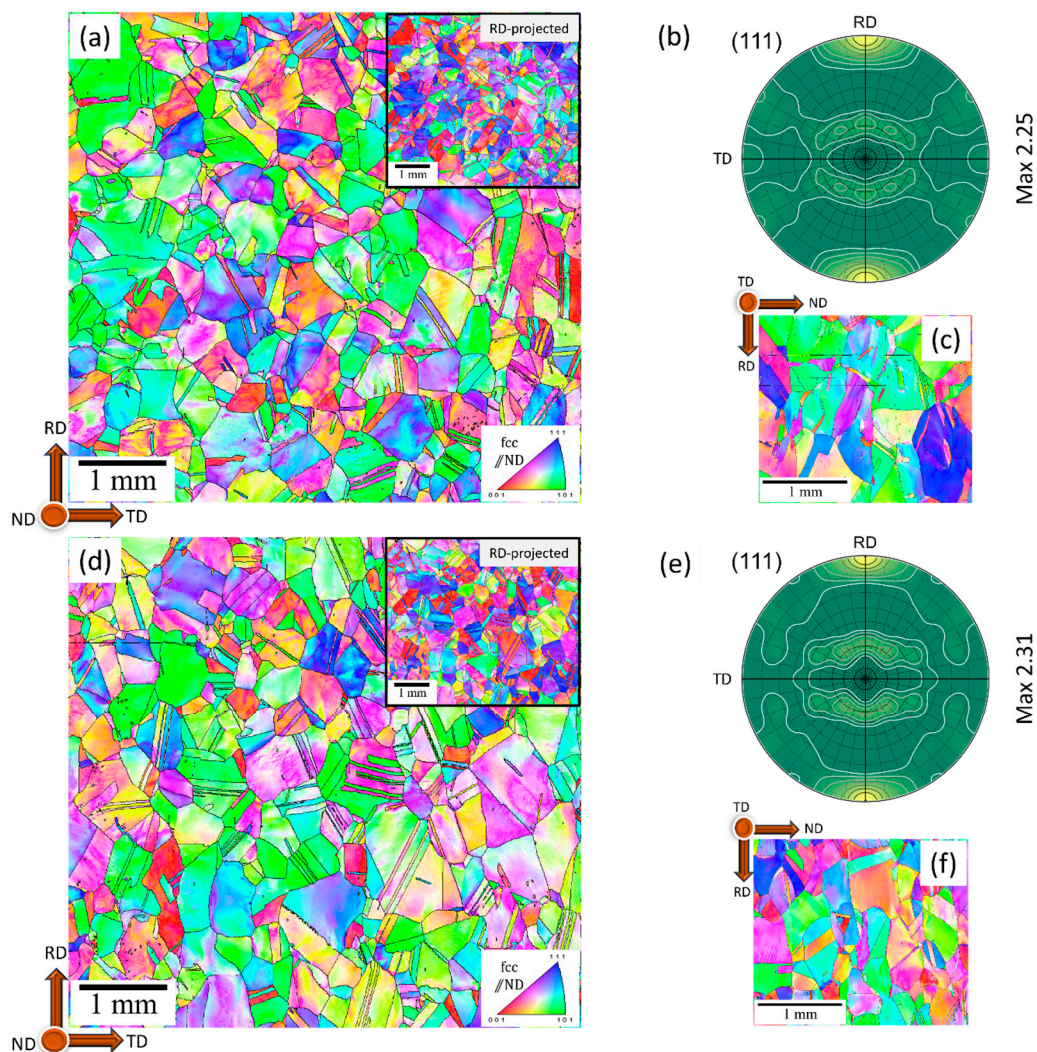


**Figure 12.** (a,d) RD-TD IPFs, (b,e) 111 pole figures, and (c,f) ND-RD IPFs corresponding to the D20 and D20A specimens, respectively.

However, when stress is applied to D20, a rotation of individual FCC grains occurs to align their slip direction with ND (loading direction). Small orientations near  $\langle 111 \rangle$  and  $\langle 001 \rangle // \text{RD}$  are also observed in the RD-projected IPFs of Figure 12a. The slip mode of deformation in FCC alloy predominantly occurs in the most densely packed planes, i.e.,  $\{111\}$ , as shown in Figure 13a for D50 (50% deformed). This rotation becomes more intense with increasing deformation, resulting in stronger texture in D50 compared to D20, as observed by the corresponding pole figures in Figures 12b and 13b. The (111) poles' maximum intensity increased from 2.25 to 2.96 'times random' as deformation increased from 20% to 50%.

Additionally, the deformation mechanism appears to enhance the internal structure within the grains through the continuous generation of dislocations, as illustrated in Figures 12a,d and 13a,d. This can be observed by comparing the individual coarse and equiaxed grains (Figure 11c,f) to the deformed crystals that are elongated towards the RD (Figure 12c,f and 13c,f) in ND-RD IPFs. Apart from this morphological change, the crystals' orientation gradient after rolling indicates that each grain underwent a non-uniform magnitude of rotation, as the crystals' degree of freedom in different points can be mechanically limited by their boundaries. When the slip runs on several crystals simultaneously, a messy and inhomogeneous structure known as deformation bands, as shown in Figure 13a,c, can be generated. The density of deformation bands increased by

up to 50% due to rolling reduction. The annealing twins appeared bent or even vanished as the degree of plastic deformation increased.

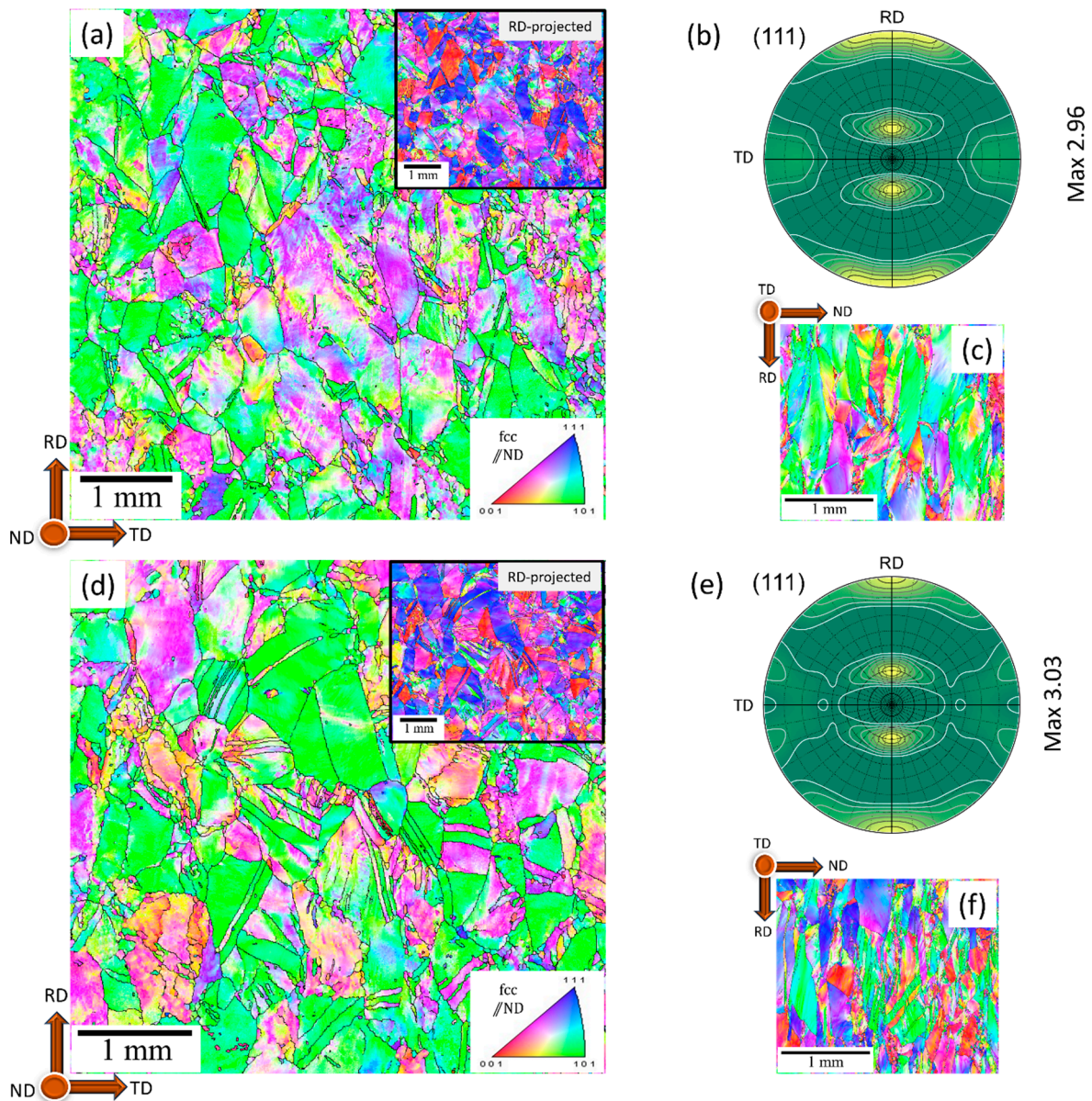


**Figure 13.** (a,d) RD-TD IPFs, (b,e) 111 pole figures, and (c,f) ND-RD IPFs corresponding to the D50 and D50A specimens, respectively.

From the IPFs and pole figures in the aged conditions of D20A and D50A shown in Figures 12d–f and 13d–f, it can be inferred that their major initial preferred orientations were preserved. Further analyses are necessary to identify the detailed texture evolution before and after the heat treatment because pole figures may not differentiate texture components properly.

#### Evolution of texture

The ideal positions of basic texture components developed for cold-rolled FCC materials are schematically represented in the ODF sections of  $\phi_2 = 0^\circ$ ,  $45^\circ$ , and  $63^\circ$  in Figure 14 for clarity.

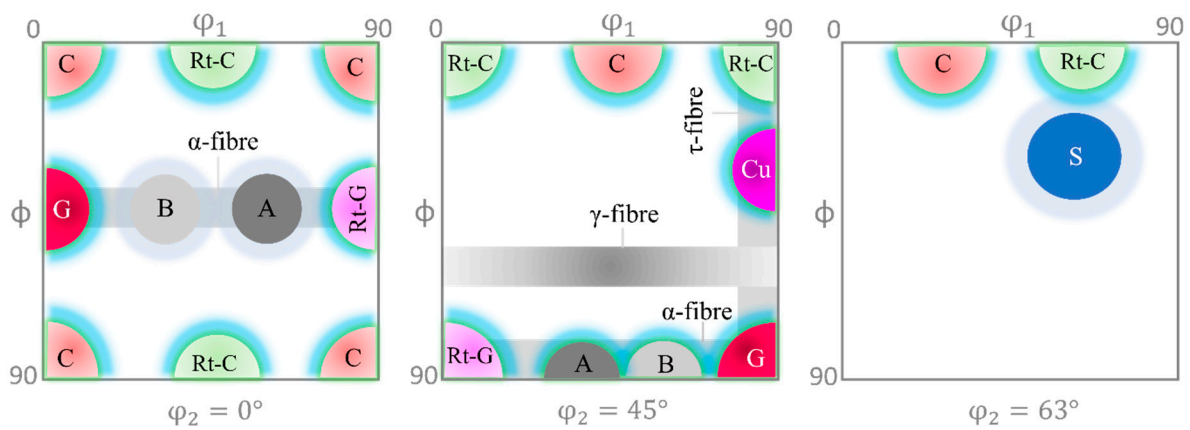


**Figure 14.** Schematic display of typical texture components in rolled FCC materials.

Table 2 lists the identified orientations expressed by their Miller indices and corresponding Euler angles. Combined with the schematic representation of the basic micro-textural components, Goss (G):{110}<001>, Brass (B):{110}<112>, Copper (Cu):{112}<111>, S:{123}<634>, A:{110}<111>, and G/B:{110}<114> were the major preferred orientations in this work. The resulting textures are shown in Figure 15. The calculated ODFs in Figure 15a,c clearly demonstrate a more textured material at a higher degree of deformation, as also expected based on the orientation maps. In addition to the magnitude of rolling deformation, any changes in the rolling temperature as well as in the chemical composition, mechanical and thermal history, etc., may reflect on the formation of texture [32]. Assuming the constant working temperature (ambient temperature), chemical composition, and initial texture in this case, the magnitude of deformation and the aging treatment are the only influencing factors on the preferred orientation discussed here.

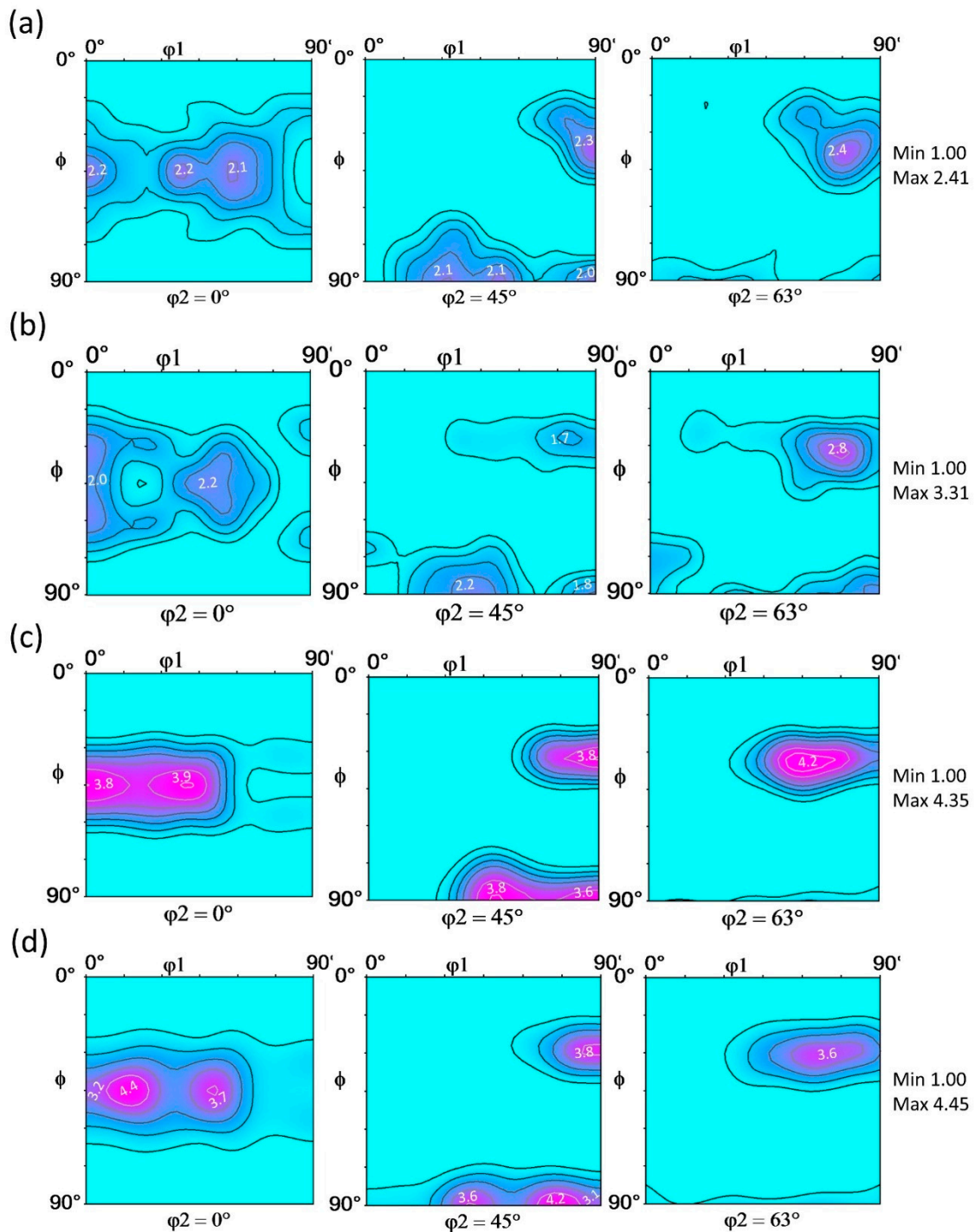
**Table 2.** Type and crystallography details of characterized texture components.

Type	Miller Indices	Euler Angles			Fiber
		$\phi_1$	$\phi$	$\phi_2$	
Brass (B)	{110}<112>	55	90	45	$\alpha/\beta$
Copper (Cu)	{112}<111>	90	35	45	$\beta$
S	{123}<634>	59	37	63	$\beta$
Goss	{110}<001>	90	90	45	$\alpha$
A	{110}<111>	35	90	45	$\alpha$
G/B	{110}<114>	20	45	0	$\alpha$

Upon examining the ODF sections  $\phi_2 = 0^\circ$  in Figure 15a–d, it is evident that the rolling textures are oriented in a family of directions due to the previously identified <110>//ND alignment. Across all specimens, an  $\alpha$ -fiber tends to form, ideally stretching from G:{110}<001> to Rot-G:{110}<011>. However, in D20, the fiber appears faded and depressed due to the existing orientations of B:{110}<112> and G:{110}<001> and an orientation close to A:{110}<111>, which have similar intensities. In D50, the material is more plastically deformed, causing the  $\alpha$ -fiber to lack the intensity of {110}<111> but appear more stretched and continuous, as shown in Figure 15c. The primary fiber constituents, {110}<001> and {110}<112>, in D50 are almost doubled in strength compared to those in D20.

In this study, it was observed that Cu:{112}<111> and S:{123}<634> were the primary deformation textures in the ODF sections  $\phi_2 = 45^\circ$  and  $\phi_2 = 63^\circ$ , respectively, as depicted in Figures 6c and 15a. Despite this, S:{123}<634> exhibited one of the highest strengths in all of the as-deformed and aged conditions. This texture lies on the second tube of

orientation ( $\beta$ -fiber), which extends from Cu: $\{112\}\langle 111\rangle$  to B: $\{110\}\langle 112\rangle$  and intersects with S: $\{123\}\langle 634\rangle$  in the 3D Euler space. As a result, two families of deformation textures,  $\alpha$  and  $\beta$ -fibers, were characterized.



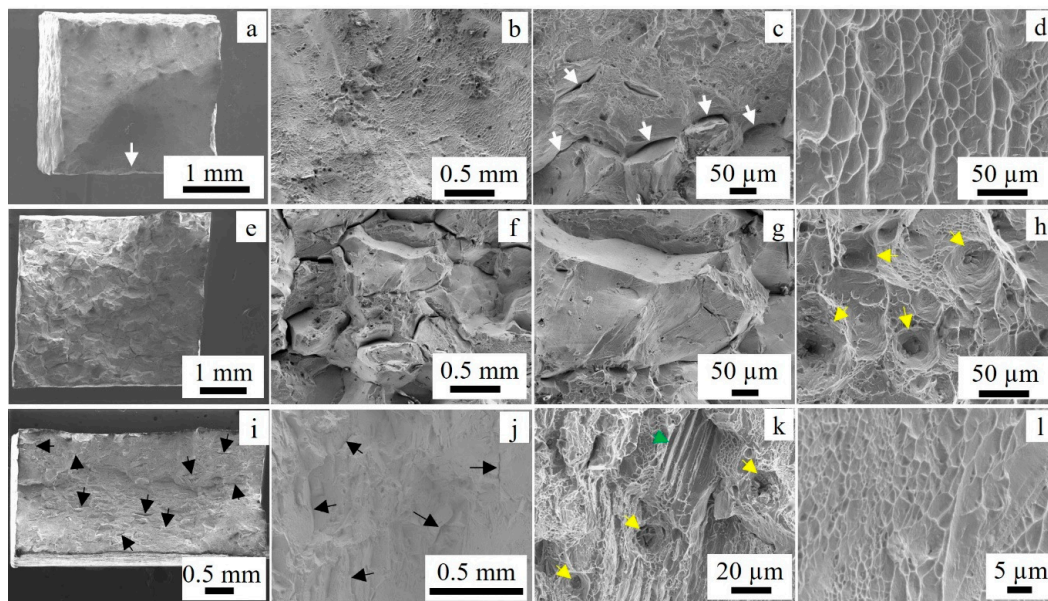
**Figure 15.** ODF sections of  $\phi_2 = 0^\circ$ ,  $45^\circ$ , and  $63^\circ$  calculated for (a) D20, (b) D20A, (c) D50, and (d) D50A.

Figure 15b,d show that aging has a minor effect on the crystallographic properties of the material, especially in the less-deformed state (D20A) compared to the non-aged state (Figure 15a,c). The fiber nature of the texture remains similar, with slight variations in intensity compared to the as-rolled state. However, in highly deformed specimens (D50A), the strong  $\alpha$ -fiber splits, leading to the decomposition of the sharp texture continuity. This

is evident in the 4.4 times random of  $G/B:\{110\}\langle 114\rangle$  in ODF section  $\phi_2 = 0^\circ$  in Figure 15d. Additionally, the orientation  $\{110\}\langle 112\rangle$  is reduced, and the intensity of  $\{110\}\langle 001\rangle$  drops to 3.2 times random, which can also be observed in the 111 poles' positioning of Figure 13f. Furthermore, the magnitude of  $\{123\}\langle 634\rangle$  in  $\phi_2 = 63^\circ$  decreases to 3.6 times random after the aging heat treatment.

### 3.6. Fracture Surface Analysis

The following is a description of the SEM images that demonstrate the fracture surfaces of the tensile specimens presented in Figure 16. The first specimen, D0A, which is undeformed and aged, displays ductile characteristics with a few intergranular fractures. There are also some tiny microvoids, but elongated dimples dominate most of the fracture.



**Figure 16.** Tensile fracture morphology of (a–d) D0A, (e–h) D20A, and (i–l) D50A. The white arrows in (c) are pointing to microcracks near the edge; the black arrows in (i,j) are pointing to some of the transgranular cracks in D50A; and (h) indicates some of the micropores. Shallow dimples are seen in certain locations of D50 (l). The black arrows are pointing to microcracks, the yellow arrows are pointing to microvoids, the white arrows point to intergranular-type cracks, and the green arrows point to shear-type cracks.

The next specimen, D20A, which is 20% deformed and aged, mainly exhibits intergranular fractures that can be several micrometers long. Some parts of the fracture also show clean surfaces without dimples. A magnified view of one of these areas is presented in Figure 16g. In addition, D20A presents large and deep microvoids, which could be cleavage facets corresponding to crystal planes, as shown by the yellow arrows in Figure 16h. Both D20A and D50A display faceted features rather than dimples. The existence of facets and shear implies that localized brittle failure is responsible for the shorter elongation observed in the deformed specimens, particularly in D50A.

## 4. Discussions

### 4.1. Effect of Cold Rolling on Hardening Precipitates

As shown in the previous sections, the process of cold rolling alters the nucleation, morphology, and distribution of the hardening precipitates compared to the unrolled state. The nucleation sites of the  $\gamma''$  and  $\gamma'$  phases were found to be predominantly located in the strained regions rather than the strain-free areas (as shown in Figure 7f). The strained regions exhibit a high density of dislocations that trap atoms. The motion of Nb, the primary constituent element of the  $\gamma''$  and  $\gamma'$  phases, which is also the heaviest element

in alloy 718, can be halted by dislocations. Therefore, the initiation of nucleation of  $\gamma''$  precipitates at dislocation-rich areas in the deformed specimens, particularly in D50A, is not unexpected. This agrees with the findings of Mei and co-workers [21] who found the nucleation of the  $\gamma''$  phase near the pre-existing dislocations based on the Differential Scanning Calorimetry (DSC) measurement.

In the 50% deformed specimens, the size of the precipitates was smaller compared to those formed in the undeformed specimen. The average size of the precipitates in the 50% deformed specimens was  $8.2 \pm 1.6$  nm, while it was  $9.5 \pm 2.1$  nm in the undeformed specimens. Similarly, the average size of the precipitates in the 20% deformed specimens was  $12.6 \pm 3.2$  nm, about 3 nm larger than that of the undeformed specimens. The growth or coarsening of the precipitates can only occur if more Nb atoms come to the nucleation sites. However, the high density of dislocations in the neighborhood forms barriers to prevent the further incoming of Nb atoms. The fact that  $\gamma''$  precipitates appeared needle/rod-like in morphology implies a shortage of Nb atoms for growth to an ellipsoid shape. From the results, it appears that cold rolling to a moderate level (about 20%) facilitates the nucleation and coarsening of  $\gamma''$  than at a higher deformation level. By increasing deformation to 50%, the size as well as the quantity of  $\gamma''$  precipitates appear to diminish.

#### 4.2. Effects of Cold Rolling on Hardness and Tensile Properties

The process of cold rolling significantly alters the mechanical strength of Inconel 718. However, it reduces its ductility, which can be explained by changes in the microstructure and precipitation hardening phases. The hardness of the specimens rolled and aged at 20% (D20A) and 50% (D50A) increased by approximately 42 HV (10%) and 98 HV (23%), respectively, compared to D0A (undeformed but aged). To identify the factors that affect hardness, we revisit the approach of Mei and colleagues [21], which distinguishes the main factors affecting hardness using the empirical formula given in Equation (1) [21].

$$HV = HV_S + HV_{WH} + HV_{PH} \quad (1)$$

The subscripts S, WH, and PH in the formulation stand for solid solution heat treatment, work hardening, and precipitation hardening, respectively. According to Figure 9, the hardness value of the specimen following the solid solution (D0) is 165 HV. By substituting the measured values in Equation (1), the hardness values for the three cases can be estimated as shown in Equations (2)–(4). It is worth noting that the effects of recovery during aging were not considered.

$$HV_{D0A} = 165 + 0 + 275 = 430 \quad (2)$$

$$HV_{D20A} = 165 + 126 + 181 = 472 \quad (3)$$

$$HV_{D50A} = 165 + 252 + 111 = 528 \quad (4)$$

It has been observed that the hardness of Inconel 718 increases as the percentage of deformation increases. For instance, the hardness of a specimen deformed by 50% is twice as much as that of a specimen deformed by 20%. However, as the percentage of deformation increases, the contribution of precipitation hardening to the hardness decreases. In comparison to the 20% deformed specimen, the hardness of the 50% deformed specimen decreased by about 63% (70 HV). This observation is similar to what was reported by Mei et al. [21]. They noted an increase in  $HV_{WH}$  and a reduction in  $HV_{PH}$  by increasing the level of rolling from 0% to 70%. Overall, D50A attains the highest hardness compared to D20A and D0A. For moderate deformation (in this case, 20%), the contribution of precipitation hardening is larger than that due to work hardening. This may indicate that a lower density of dislocations occurred compared to the 50% deformed specimen. Consequently, work hardening was the main contributor to the highest hardness achieved in D50A.

The empirical formula used for measuring hardness can also be used to determine the effects of rolling on tensile properties. In this case, since tensile tests were not performed for ST specimens (D0), the first term on the right side of Equation (1) can be omitted, and the equation can be rewritten for the UTS by substituting the numerical values provided in Figure 10.

$$\text{UTSD0A} = 1132 + 0 \quad (5)$$

$$\text{UTSD20A} = 1132 + 216 \quad (6)$$

$$\text{UTSD50A} = 1132 + 513 \quad (7)$$

Equations (5)–(7) indicate that as the level of deformation increases, the tensile strength also increases. When the specimen was deformed by 20% (D20A), the UTS increased by 216 MPa (19%) compared to the undeformed specimen (D0A). When the specimen was deformed by 50% (D50A), the UTS increased by 513 MPa (45%). The yield strength also followed a similar trend, with deformation enhancing the yield strength by 242 MPa (25%) for a 20% reduction and by 552 MPa (58%) for a 50% reduction. The increase in the yield strength was more pronounced than that of the UTS for both deformations. The presence of nanotwins might have contributed to the enhanced elastic property of the specimens. Furthermore, the concentration of nanotwins in D50A was found to be higher than that in D20A, indicating a qualitative difference between the two specimens.

The tensile properties obtained from our recent work are generally better than what has been reported in the literature, especially under the same conditions of heat treatments and rolling that produced the  $\delta$  phase. Under a 50% deformed condition, our work showed a maximum UTS of 1645 MPa, a maximum yield strength (YS) of 1512 MPa, and an elongation of 3.8%. On the other hand, the 20% deformed specimen displayed a UTS of 1348 MPa, a YS of 1202 MPa, and an elongation of 11%.

The relationship between tensile properties and deformation can be linked to the degree of changes in the microstructure. To comprehend the mechanism of deformation during cold rolling, TEM analysis can be used. Figure 17 depicts the TEM images of the specimens that were made from the RD-ND surface. The BF (a), DF (c, d), and indexed diffraction pattern (b) exhibit the existence of a high density of twin lamellas ranging from a few nanometers to several micrometers. As illustrated in the images in Figure 17, the twins are stacked together in localized bands that are perpendicular to ND-RD. These nano/microtwins are known to be robust and impenetrable barriers for dislocation slips, as disclosed in the literature [40]. The small spacing between the twin lamellae significantly reduces the mean free path for dislocation slip. Therefore, the twins enhance the high strain-hardening rates during cold rolling [41] in addition to dislocations and other lattice defects.

#### 4.3. Effects of Cold Rolling on Texture

Crystallographic textures have a significant impact on the mechanical, physical, and chemical properties of alloys. Depending on the value of stacking fault energy ( $\gamma_{\text{SFE}}$ ) of the FCC materials, two common categories of rolling textures can be identified: alloy type and pure metal type. The former is associated with low  $\gamma_{\text{SFE}}$  materials and promotes a strong B orientation along with a weak G. On the other hand, the latter is typically found in medium-to-high  $\gamma_{\text{SFE}}$  materials and has the same intensities of Cu, S, and B orientations [42]. In this work, the formation of Cu, S, and B on  $\beta$ -fiber and their intensities were enhanced under a higher deformation, which can be linked to Ni's high  $\gamma_{\text{SFE}}$ . The cross-slip of screw dislocations leads to the development of a dominant pure metal texture. However, a decrease in the value of  $\gamma_{\text{SFE}}$  due to solute elements can result in an alloy-type texture predominantly induced by mechanical twinning, which may affect the intensity of B and the production of G. Assuming the binary system contribution of each element and Ni, and the least influence of Fe, the decrement in  $\gamma_{\text{SFE}}$  can be roughly estimated based on the composition of the Inconel 718 alloy [43]:

$$\Delta\gamma_{\text{SFE}} \% = 1.66 (\text{at. \%Cr}) + 1.72 (\text{at. \%Al}) + 8.0 (\text{at. \%Ti}) + 1.66 (\text{at. \%Mo}) + 50\% (\text{at. \%W, if the contribution of W is } > 0.65) + 0.26 (\text{at. \%Co}) \quad (8)$$

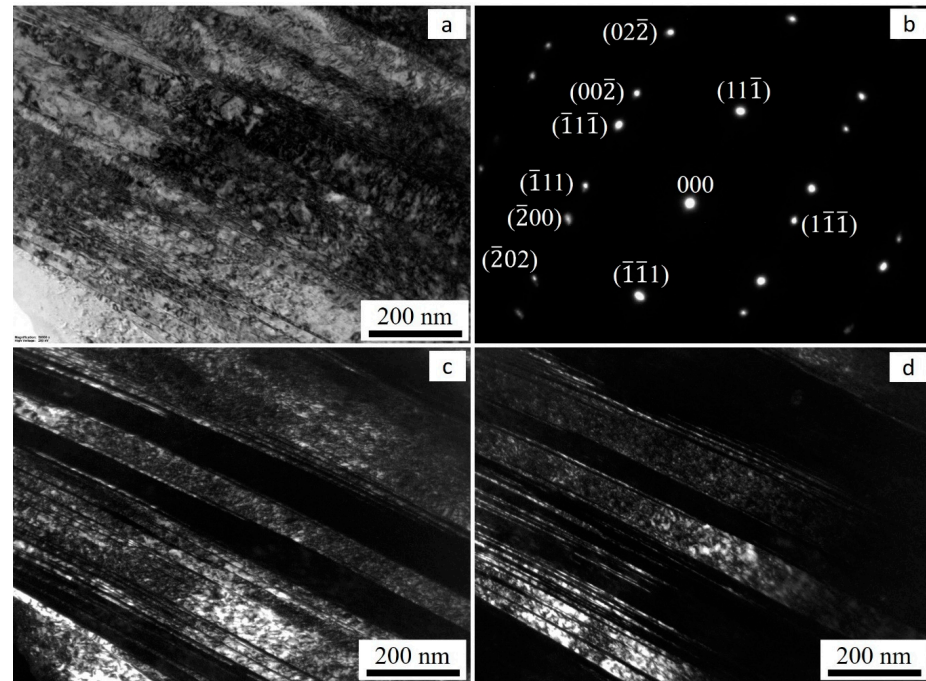


**Figure 17.** TEM images of specimens that were cold-rolled and aged by 50% (D250A) on the RD-TD surface. (a) Bright field (BF) image, (b) SADP in the  $\langle 110 \rangle$  zone axis, (c) dark field (DF) image of the first set of twins (00-2), and (d) DF image of the second set of twins using  $\{-11-1\}$  reflection.

The high concentration of Cr, along with the presence of Mo, Co, Ti, and Al, can significantly reduce the  $\gamma_{\text{SFE}}$ . In this case, the  $\gamma_{\text{SFE}}$  of the alloy dropped to a medium level of  $67.5 \text{ mJm}^{-2}$  after an estimated  $\Delta\gamma_{\text{SFE}}$  of 42.27%. As a result, the solid-solution-strengthened Inconel 718 alloy may be highly susceptible to deformation under the twinning mechanism, which could lead to the production of an alloy-type texture. This results in the formation of an  $\alpha$ -fiber that is predominantly stretched between  $\{110\}\langle 001 \rangle$  and  $\{110\}\langle 112 \rangle$ .

## 5. Conclusions

The aim of this study was primarily to analyze the impact of the cold rolling process on the hardness and tensile properties of Inconel 718. It was observed that the deformation caused by cold rolling led to a considerable increase in both the tensile strength and hardness but caused a reduction in ductility. In summary, the results of this study indicate the following:

- The size of the  $\gamma''$  precipitate, which is the main PH phase, increased when subjected to 20% deformation but decreased after 50% deformation and took on a pin/rod-like shape.
- The cold rolling process increased the hardness of the 20% deformed specimens (D20A) by approximately 42 HV (10%), and for the 50% deformed specimens (D50A), the hardness increased by 98 HV (23%).
- The UTS also increased after deformation, with a 19% (216 MPa) increment for the 20% deformed specimens (D20A) and a 45% (513 MPa) increment in the UTS for the 50% deformed specimens (D50A).
- The material strength increases with an increasing percentage of deformation, where the contribution of precipitation hardening decreases while that of work hardening

increases. These changes can be attributed to the further strained microstructure due to the formation of dislocations and micro-twinning.

- When a 50% deformation is applied, the tensile strength (UTS and YS) is significantly high, but the elongation at failure is very low and requires modification. To achieve a balanced tensile property, a moderate deformation level of 20% is recommended.
- Both pure-metal-type and alloy-type textures started to form under cold rolling, and their magnitudes were further enhanced at a higher deformation. The former generated the  $\beta$ -fiber, consisting of  $\{110\}\langle 112\rangle$ ,  $\{112\}\langle 111\rangle$ , and  $\{123\}\langle 634\rangle$ , which are induced by the cross-slip mechanism of dislocations. The latter was shown to be developed by the reduction in the stacking fault energy and led to the twinning-induced orientation emerged by a predominant  $\langle 110\rangle$  // ND, so-called  $\alpha$ -fiber.
- After the aging treatment, no significant changes were observed in the crystallographic nature of the material, except for minor variations in the intensities.

**Author Contributions:** Conceptualization, W.M.T., N.S. and V.H.; Formal Analysis, W.M.T. and A.T.S.; Investigation, W.M.T., A.T.S. and N.S.; Methodology, W.M.T., A.T.S., N.S. and V.H.; Resources, V.H.; Supervision, W.M.T. and V.H.; Writing—Original Draft, W.M.T., A.T.S. and N.S.; Writing—Review and Editing, W.M.T., A.T.S., N.S. and V.H. All authors have read and agreed to the published version of the manuscript.

**Funding:** This research received no external funding.

**Data Availability Statement:** The raw data supporting the conclusions of this article will be made available by the authors on request.

**Acknowledgments:** The authors express their gratitude to Scandinavian Fittings and Flanges for providing the specimens used in this study. Additionally, the second author would like to thank Johan Andreas Håland Thorkaas and Espen Undheim for their valuable assistance in the labs during his M.Sc. project.

**Conflicts of Interest:** Author Anders Thon Sletsjøe was employed by the company Vipe 21 AS. The remaining authors declare that the research was conducted in the absence of any commercial or financial relationships that could be construed as a potential conflict of interest.

## References

1. Ran, R.; Wang, Y.; Zhang, Y.-X.; Fang, F.; Wang, H.-S.; Yuan, G.; Wang, G.-D. Microstructure, precipitates and mechanical properties of Inconel 718 alloy produced by two-stage cold rolling method. *Mater. Sci. Eng. A* **2020**, *793*, 139860. [\[CrossRef\]](#)
2. Ran, R.; Wang, Y.; Zhang, Y.-X.; Fang, F.; Xia, Y.-K.; Zhang, W.-N.; Yuan, G.; Wang, G.-D. Two-stage annealing treatment to uniformly refine the microstructure, tailor  $\delta$  precipitates and improve tensile properties of Inconel 718 alloy. *J. Alloys Compd.* **2022**, *927*, 166820. [\[CrossRef\]](#)
3. Donachie, M.J.; Donachie, S.J. *Superalloys: A Technical Guide*; ASM International: Almere, The Netherlands, 2002.
4. Qi, H.; Azer, M.; Ritter, A. Studies of Standard Heat Treatment Effects on Microstructure and Mechanical Properties of Laser Net Shape Manufactured INCONEL 718. *Metall. Mater. Trans. A* **2009**, *40*, 2410–2422. [\[CrossRef\]](#)
5. Cozar, R.; Pineau, A. Morphology of  $\gamma'$  and  $\gamma''$  precipitates and thermal stability of inconel 718 type alloys. *Metall. Trans.* **1973**, *4*, 47–59. [\[CrossRef\]](#)
6. Sundararaman, M.; Mukhopadhyay, P.; Banerjee, S. Some aspects of the precipitation of metastable intermetallic phases in INCONEL 718. *Metall. Trans. A* **1992**, *23*, 2015–2028. [\[CrossRef\]](#)
7. Paulonis, D.; Oblak, J.; Duvall, D. *Precipitation in Nickel-Base Alloy 718*; Defense Technical Information Center: Fort Belvoir, VA, USA, 1969.
8. Tucho, W.M.; Hansen, V. Characterization of SLM-fabricated Inconel 718 after solid solution and precipitation hardening heat treatments. *J. Mater. Sci.* **2019**, *54*, 823–839. [\[CrossRef\]](#)
9. Gao, Y.; Zhang, D.; Cao, M.; Chen, R.; Feng, Z.; Poprawe, R.; Schleifenbaum, J.H.; Ziegler, S. Effect of  $\delta$  phase on high temperature mechanical performances of Inconel 718 fabricated with SLM process. *Mater. Sci. Eng. A* **2019**, *767*, 138327. [\[CrossRef\]](#)
10. *API Standard 6A718*; Nickel Base Alloy 718 (UNS N07718) for Oil and Gas Drilling Production Equipment. API Publishing Services: Washington, DC, USA, 2009.
11. Chen, Y.-T.; Yeh, A.-C.; Li, M.-Y.; Kuo, S.-M. Effects of processing routes on room temperature tensile strength and elongation for Inconel 718. *Mater. Des.* **2017**, *119*, 235–243. [\[CrossRef\]](#)
12. Ye, N.-y.; Zhang, G.-l.; Huang, T.Y.; Cheng, M.; Zhang, S.-H.; Wang, W. Orientational growth behavior and mechanism of delta ( $\delta$ ) phase precipitation in cold-rolled Inconel 718 alloy during heat treatment. *J. Iron Steel Res. Int.* **2023**, *31*, 264–274. [\[CrossRef\]](#)

13. Dai, X.; Zhuang, K.; Pu, D.; Zhang, W.; Ding, H. An Investigation of the Work Hardening Behavior in Interrupted Cutting Inconel 718 under Cryogenic Conditions. *Materials* **2020**, *13*, 2202. [[CrossRef](#)] [[PubMed](#)]
14. Wang, J.; Cheng, S.; Wu, Y.; Wang, T.; Qin, X.; Zhou, L. Effect of cold rolling on microstructure, texture, and tensile properties of a Ni-Fe-based superalloy. *J. Alloys Compd.* **2023**, *937*, 168383. [[CrossRef](#)]
15. Yang, X.; Chen, S.-n.; Wang, B.; Li, X.; Wang, B.; Tian, Y. Superplastic deformation behavior of cold-rolled Inconel 718 alloy at high strain rates. *J. Mater. Process. Technol.* **2022**, *308*, 117696. [[CrossRef](#)]
16. Zhang, J.-L.; Guo, Q.-Y.; Liu, Y.-C.; Li, C.; Yu, L.-M.; Li, H.-J. Effect of cold rolling and first precipitates on the coarsening behavior of  $\gamma''$ -phases in Inconel 718 alloy. *Int. J. Miner. Metall. Mater.* **2016**, *23*, 1087–1096. [[CrossRef](#)]
17. Liu, W.C.; Yao, M.; Chen, Z.L. Effect of cold rolling on the precipitation behavior of  $\delta$  phase in INCONEL 718. *Metall. Mater. Trans. A* **1999**, *30*, 31–40. [[CrossRef](#)]
18. Liu, W.C.; Xiao, F.R.; Yao, M.; Chen, Z.L.; Jiang, Z.Q.; Wang, S.G. The influence of cold rolling on the precipitation of delta phase in inconel 718 alloy. *Scr. Mater.* **1997**, *37*, 53–57. [[CrossRef](#)]
19. Ran, R.; Wang, Y.; Zhang, Y.-X.; Fang, F.; Xia, Y.-K.; Zhang, W.-N.; Yuan, G.; Wang, G.-D. Alleviating segregation and enhancing tensile properties of Inconel 718 superalloy by twin-roll casting and two-stage cold rolling. *J. Mater. Res. Technol.* **2022**, *20*, 1216–1225. [[CrossRef](#)]
20. Mei, Y.; Liu, C.; Liu, Y.; Zhou, X.; Yu, L.; Li, C.; Ma, Z.; Huang, Y. Effects of cold rolling on the precipitation and the morphology of  $\delta$ -phase in Inconel 718 alloy. *J. Mater. Res.* **2016**, *31*, 443–454. [[CrossRef](#)]
21. Mei, Y.; Liu, Y.; Liu, C.; Li, C.; Yu, L.; Guo, Q.; Li, H. Effects of cold rolling on the precipitation kinetics and the morphology evolution of intermediate phases in Inconel 718 alloy. *J. Alloys Compd.* **2015**, *649*, 949–960. [[CrossRef](#)]
22. Chen, S.-N.; Yang, X.; Wang, B.; Li, Z.; Gao, X.; Wang, B.; Tian, Y. Effect of deformation and annealing process on microstructure and properties of Inconel 718 foil. *Mater. Charact.* **2023**, *205*, 113322. [[CrossRef](#)]
23. Azadian, S.; Wei, L.-Y.; Warren, R. Delta phase precipitation in Inconel 718. *Mater. Charact.* **2004**, *53*, 7–16. [[CrossRef](#)]
24. Rongbin, L.; Xianchang, H.; Mei, Y.; Wenchang, L. Effects of cold rolling on precipitates in inconel 718 alloy. *J. Mater. Eng. Perform.* **2002**, *11*, 504–508. [[CrossRef](#)]
25. Zhang, Y.; Lan, L.; Zhao, Y. Effect of precipitated phases on the mechanical properties and fracture mechanisms of Inconel 718 alloy. *Mater. Sci. Eng. A* **2023**, *864*, 144598. [[CrossRef](#)]
26. Anderson, M.; Thielin, A.L.; Bridier, F.; Bocher, P.; Savoie, J.  $\delta$  Phase precipitation in Inconel 718 and associated mechanical properties. *Mater. Sci. Eng. A* **2017**, *679*, 48–55. [[CrossRef](#)]
27. Desvallees, Y.; Bouzidi, M.; Bois, F.; Beaude, N. Delta Phase in INCONEL 718: Mechanical Properties and Forging Process Requirements. *Superalloys* **1994**, 281–291.
28. deBarbadillo, J.J.; Mannan, S.K. Alloy 718 for Oilfield Applications. *JOM* **2012**, *64*, 265–270. [[CrossRef](#)]
29. Wang, Y.-Q.; Yuan, C.; Wei, J.-X.; Gao, X.-Y.; Chen, Y.-P.; Kong, W.-W.; Zhang, B.; Wen, X.; Liu, X.; Liu, S. Texture evolution and twinnability prediction of the most compliant orientation in GH3536 superalloy during cold rolling. *J. Mater. Res. Technol.* **2023**, *24*, 2743–2756. [[CrossRef](#)]
30. Zeng, M.T.; Yang, Y.; Tan, Y.B.; Zhang, W.W.; Xiang, S.; Ma, M.; Zhao, F. Recrystallization behavior and texture evolution of cryo-rolled GH159 superalloy with an ultra-high strength. *Mater. Charact.* **2023**, *197*, 112656. [[CrossRef](#)]
31. Zhang, W.W.; Yang, Y.; Tan, Y.B.; Zeng, M.T.; Ma, M.; Xiang, S.; Zhao, F. Microstructure evolution and strengthening mechanisms of MP159 superalloy during room temperature rolling and cryorolling. *J. Alloys Compd.* **2022**, *908*, 164667. [[CrossRef](#)]
32. Kestens, L.A.I.; Pirgazi, H. Texture formation in metal alloys with cubic crystal structures. *Mater. Sci. Technol.* **2016**, *32*, 1303–1315. [[CrossRef](#)]
33. Sletsjøe, A.T. Effects of Cold Rolling on the Mechanical Properties and Grain Structure of Inconel 718 Alloy. Master's Thesis, University of Stavanger, Stavanger, Norway, 2023.
34. Tucho, W.M.; Hansen, V. Studies of Post-Fabrication Heat Treatment of L-PBF-Inconel 718: Effects of Hold Time on Microstructure, Annealing Twins, and Hardness. *Metals* **2021**, *11*, 266. [[CrossRef](#)]
35. Beausir, B.; Fundenberger, J. *Analysis Tools for Electron and X-ray Diffraction, ATEX-Software*; Université de Lorraine-Metz: Metz, France, 2017.
36. AMS5662; Alloy, Bars, Forgings, and Rings, Corrosion and Heat Resistant Nickel Base-19Cr-3.1Mo-5.1(Cb+Ta)-0.90Ti-0.50Al Consumable Electrode or Vacuum Induction Melted, Solution Treated. SAE International: Warrendale, PA, USA, 2022.
37. ISO 6507-1:2018; Metallic Materials Vickers Hardness Test Part 1: Test Method. ISO: Geneva, Switzerland, 2018; p. 6.
38. ISO 6892-1:2009; Metallic Materials—Tensile Testing—Part 1: Method of Test at Room Temperature. ISO: Geneva, Switzerland, 2019.
39. Hong, S.; Chen, W.; Wang, T. A diffraction study of the  $\gamma''$  phase in INCONEL 718 superalloy. *Metall. Mater. Trans. A* **2001**, *32*, 1887–1901. [[CrossRef](#)]
40. Robinson, J.M.; Shaw, M.P. Microstructural and mechanical influences on dynamic strain aging phenomena. *Int. Mater. Rev.* **1994**, *39*, 113–122. [[CrossRef](#)]
41. Bracke, L.; Verbeken, K.; Kestens, L.; Penning, J. Microstructure and texture evolution during cold rolling and annealing of a high Mn TWIP steel. *Acta Mater.* **2009**, *57*, 1512–1524. [[CrossRef](#)]

42. Suwas, S.; Ray, R.K. Experimental Determination of Texture. In *Crystallographic Texture of Materials*; Suwas, S., Ray, R.K., Eds.; Springer: London, UK, 2014; pp. 39–71. [[CrossRef](#)]
43. Xie, X.S.; Chen, G.L.; McHugh, P.J.; Tien, J.K. Including stacking fault energy into the resisting stress model for creep of particle strengthened alloys. *Scr. Metall.* **1982**, *16*, 483–488. [[CrossRef](#)]

**Disclaimer/Publisher’s Note:** The statements, opinions and data contained in all publications are solely those of the individual author(s) and contributor(s) and not of MDPI and/or the editor(s). MDPI and/or the editor(s) disclaim responsibility for any injury to people or property resulting from any ideas, methods, instructions or products referred to in the content.